Experimental tweaking of symmetry breaking in recurrent nonlinear modulational instability

Guillaume Vanderhaegen,[1] Pascal Szriftgiser ●,[1] Alexandre Kudlinski,[1] Andrea Armaroli ●,[1]
Matteo Conforti,[1] Arnaud Mussot ●,[1] and Stefano Trillo[2]

[1]*University of Lille, CNRS, UMR 8523-PhLAM-Physique des Lasers Atomes et Molécules, F-59000 Lille, France*
[2]*Department of Engineering, University of Ferrara, 44122 Ferrara, Italy*

We show that the nonlinear stage of the universal phenomenon of modulational instability, and in particular its recurrent behavior, is deeply affected by arbitrarily weak losses. Indeed linear damping leads to spontaneous breaking of the recurrence symmetry through separatrix crossing occurring at multiple critical values of the attenuation, across which the dynamics switches between two types of recurrence exhibiting dramatic slowing down. We provide experimental evidence for this phenomenon in a fiber optics experiment designed in such a way that the effective losses can be carefully tailored by techniques based on Raman amplification.

I. INTRODUCTION

Modulational instability (MI), the exponential growth of slow periodic perturbations on top of a background wave is one of the most ubiquitous nonlinear wave phenomenon, occurring, e.g., in water waves [1,2], optics [3,4], plasmas [5], cold atom condensates [6], or topological insulators [7]. Boosted by the idea that MI can be the main triggering mechanism of forming rogue waves [8,9], a great deal of attention was devoted in the last decade to understanding the fully nonlinear stage of MI past the initial growth of the perturbation. Theoretical results obtained in the framework of the nonlinear Schrödinger equation (NLSE) [10–20] in conjunction with experiments mainly in the area of nonlinear optics [21–33] and hydrodynamics [23,32,34–37], have revealed an incredibly rich scenario. Different dynamical evolutions can emerge which range from the spontaneous appearance of coherent structures [24,27] to the controlled emergence of breathers [10,23,33,34,38], eventually competing [18] with the onset of universal automodulated structures [11,17,28]. The control of strictly periodic perturbations has also allowed us to demonstrate, besides novel regimes such as the higher-order [21] or extraordinary [32] MI, that the MI seeded by a single pair of unstable sidebands follows a fully reversible behavior featuring recurrences to the initial condition which are characteristic of a broken symmetry and its related phase-space structure ruled by the NLSE [25,26,30]. Since the return to a nearly-single-mode initial condition occurs after substantial coupling to several other modes (a comb of sideband pairs), such a regime was considered to be evocative of the Fermi-Pasta-Ulam-Tsingou (FPUT) phenomenon [39], discovered for conservative chains of nonlinear oscillators [40]. In analogy to the FPUT case [41,42], MI also exhibits a breakdown of the recurrent regime, and the transition to a thermalized state, when random amplification of fluctuations in the continuum of unstable modes become dominant [27,43]. The aim of this paper is to show experimentally that the ideal dynamics of the MI recurrent regime is qualitatively altered by the most common and usually unavoidable of the

perturbations, namely, *linear damping*. We show that arbitrarily weak losses cause the recurrence to undergo a dynamical change from one type to the other, through a phenomenon of loss-induced *separatrix crossing*. Remarkably, we find by perturbative arguments (based either on Fourier mode truncations or finite-gap theory [44,45]) that this crossing occurs around multiple critical values of the linear damping coefficient (the weaker the loss, the denser the critical attenuations). We demonstrate this by reporting evidence for the first two critical loss values in a fiber optics experiment, where we reconstruct via nondestructive measurements the nonlinear evolution of MI in power and phase. The observation of separatrix crossing is extremely challenging even for simple one-dimensional (1D) oscillators, due to the difficulty of controlling the damping. We overcome this problem by careful tailoring the effective losses via Raman amplification techniques [46–48], thus allowing for a reproducible laboratory observation of damping-induced separatrix crossing in an infinite-dimensional system. Our results give evidence that weak losses qualitatively alter the recurrent scenario without suppressing the MI [49] and establish a framework to understand the impact of damping on MI experiments in other areas (see, e.g., Ref. [35]), or different models [50–52].

The paper is organized as follows: in Sec. II we briefly outline the theory of the phenomenon, referring the interested reader to Appendix A for details of the calculations. Section III reports the results of the experiments. The results are summarized in Sec. IV, and in Appendix B we make a comparison with a one-dimensional oscillator.

II. THEORY OF SEPARATRIX CROSSING

We start from the NLSE with damping written in dimensionless form,

$$i\frac{\partial \psi}{\partial z} + \frac{1}{2}\frac{\partial^2 \psi}{\partial t^2} + |\psi|^2\psi = -i\frac{\alpha}{2}\psi, \tag{1}$$

where $\psi = E/\sqrt{P_0}$, $z = Z/Z_{nl}$, $t = (T - Z/V_g)/T_0$ are the normalized field, distance, and retarded time (capital letters
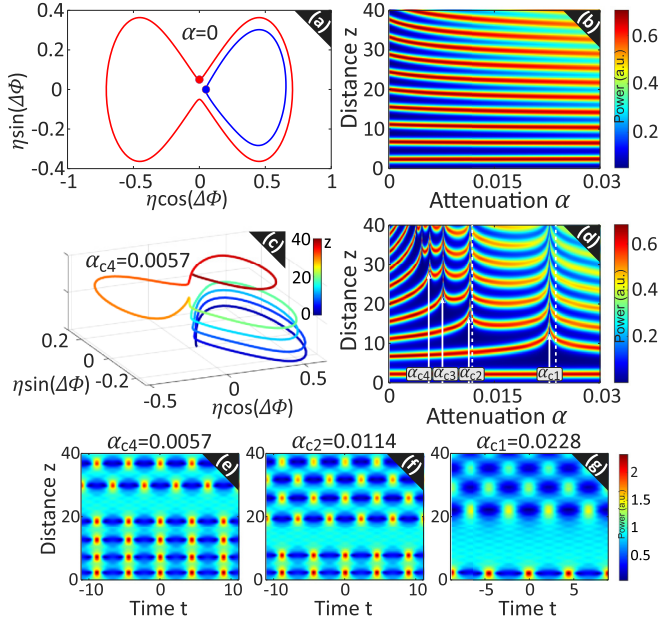
FIG. 1. (a) NLSE unperturbed ($\alpha = 0$) evolutions of unshifted (blue) and shifted (red) FPUT type, projected over the phase-plane ($\eta \cos(\Delta\phi), \eta \sin(\Delta\phi)$) (dots are initial conditions). False color plot of sideband power fraction η in the plane (α, z) for initial values on (b) the shifted or (d) unshifted orbit. The arrows in (d) indicate critical losses α_{cn} around which separatrix crossing occurs; vertical dashed lines are estimates of $\alpha_{c1,c2}$ from Eq. (A15). (c) Typical separatrix crossing in 3D space ($\eta \cos(\Delta\phi), \eta \sin(\Delta\phi), z$) at α_{c4}, cf. case (e). (e)–(g) Evolution of $|\psi(z,t)|$ at sampled values α_{c1}, α_{c2}, and α_{c4}. In all plots $\omega_0 = \sqrt{2}$ (peak gain), and the injected sideband power fraction is 5% ($\eta_0 = 0.05$).

stand for real-world quantities), in units of total input power P_0 and the associated nonlinear length $Z_{nl} = 1/(\gamma P_0)$ and time $T_0 = \sqrt{|\beta_2|Z_{nl}}$, respectively. Here γ is the fiber nonlinear coefficient, β_2 is the dispersion, and V_g the group-velocity. The key parameter is the normalized attenuation coefficient $\alpha = \alpha_P Z_{nl}$ (km)/4.34 where α_P (dB/km) is the physical attenuation.

We consider FPUT arising from induced MI which is ruled by Eq. (1) subject to the initial condition

$$\psi_0 = \sqrt{p}\left[1 + \frac{a}{\sqrt{2}}e^{-i\phi_0}(e^{i\omega_0 t} + e^{-i\omega_0 t})\right], \quad (2)$$

where, without loss of generality, we take a $\sqrt{p}$ amplitude pump modulated by symmetric sidebands with normalized input pulsation $\omega_0 = 2\pi f_{mod}\sqrt{|\beta_2|/(\gamma P_0)}$ (in the range $1 < \omega_0 < 2\sqrt{p}$ to have only one unstable pair [21]), relative power $a^2 \ll 1$, and phase ϕ_0, with $p \equiv (1 + a^2)^{-1}$ to have $\int |\psi_0|^2 dt = 1$. In the unperturbed case ($\alpha = 0$), two different FPUT types of recurrence coexist, as conveniently illustrated in Fig. 1(a) by their projections on the phase-plane ($\eta \cos \Delta\phi, \eta \sin \Delta\phi$), where $\eta(z)$ is the first-order sideband power fraction and $\Delta\phi(z) = \phi_P - \phi_S$ is the relative phase between the pump and the sidebands [25]. We refer to the two types of FPUT orbits as unshifted (single loop, blue curve) or shifted (double loop, red curve) recurrence, since in the latter case, owing to the free running phase, two

consecutive recurrences exhibit a shift of π (half period in time) [25].

In the unperturbed case the two orbits never cross each other in phase plane and are separated by a time-periodic solution which asymptotically tends to the pump or background at $z = \pm\infty$, and is known as Akhmediev breather [53,54] (see also pioneering work on the breathers with finite background of the NLSE in Ref. [55]). They are typically generated by inputs corresponding to the dots in Fig. 1(a) representing weak modulations of the pump (i.e., the saddle point in the origin) with constant sideband fraction $\eta(z = 0) = \eta_0 = a^2/(1 + a^2)$, but different phase, $\Delta\phi_0 = 0$ (amplitude modulation) or $\Delta\phi_0 = \pm\pi/2$ (frequency modulation), respectively. A convenient way to assess the impact of the losses is to portray, as shown in Figs. 1(b) and 1(d), the evolution of the sideband fraction $\eta(z)$, as obtained from numerical integration of the damped NLSE, as a function of the attenuation α. The periodicity in the vertical z direction accounts for the FPUT recurrence. When the shifted orbit is excited, the net effect of damping is smooth, inducing only a slight reduction of the FPUT period, as evident from Fig. 1(b). Conversely, an initially unshifted orbit results in the complex scenario displayed in Fig. 1(d). It is characterized by a succession of critical attenuation values α_{cn}, $n = 1, 2, 3, \dots$ (with $\alpha_{c1} > \alpha_{c2} > \alpha_{c3} \cdots$), around which the FPUT recurrence slow down dramatically giving rise to extremely large (but still finite) recurrence distances. The underlying mechanism is the dynamical *separatrix crossing* from unshifted to shifted orbits which takes place, for any loss coefficient $\alpha_{cn} \leqslant \alpha < \alpha_{c(n-1)}$, at the closest passage to the initial condition after n unshifted recurrences are completed. Conversely, for $\alpha_{c(n+1)} \leqslant \alpha < \alpha_{cn}$ also the $(n + 1)$st recurrence will be still unshifted and crossing occurs at the $(n + 2)$nd recurrence. This is conveniently illustrated, for $\alpha = \alpha_{c4}$, by the phase-space projection in Fig. 1(c), where four unshifted revolutions are clearly visible along with the slowing down in the fourth passage close to the origin which precedes the crossing. For better clarity, Figs. 1(e)–1(g) further show examples of spatiotemporal evolutions obtained at the critical values α_{c4} [same as in Fig. 1(c)] and α_{c2} and α_{c1}, showing indeed the appearance of the phase shift after $n = 4$ or $n = 2, 1$ recurrences, respectively. It must be noticed also that the growth and decay cycles do not proceed at constant rate but slow down considerably when approaching the saddle point (i.e., at the return to the initial condition). This effect is strongly enhanced at the critical values α_{cn}, which is such that the evolution becomes locally iso-energetic (i.e., same local Hamiltonian) to the saddle in its closest passage after n unshifted orbits. This argument allows us to give, in the framework of a generalized three-mode approximation [25,56,57], the critical values α_{cn} as the implicit solutions of the following integral equation:

$$H_0 = \frac{\alpha_{cn}\omega_0^2}{2}\int_0^{nz_{per}} e^{\alpha_{cn}z}\eta(z)dz, \quad (3)$$

where $H_0 = \eta_0(1 - \eta_0)\cos 2\Delta\phi_0 + (1 - \omega_0^2/2)\eta_0 - \frac{3}{4}\eta_0^2$ is the input three-wave Hamiltonian [25], and z_{per} is the period of the unperturbed unshifted orbit. Equation (3) gives a quantitatively accurate estimate of the critical losses in the context of the three-wave approach. This thus validates the
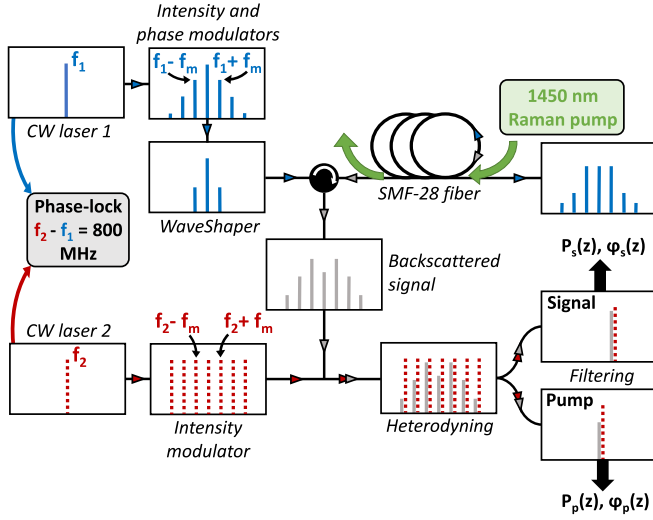
FIG. 2. Simplified sketch of the experimental setup. f_1 is the frequency of the main laser and f_2 of the phase-locked local oscillator, detuned by $f_2 - f_1 = 800$ MHz. f_m is the modulation frequency, set here at 38.2 MHz. The 1450 nm Raman pump is injected through the fiber end, and counterpropagates with respect to the main signal.

physical picture discussed above but shows discrepancy with the values obtained from the NLSE. This is due to the fact it underestimates the evolution period z_{per}, which is a critical parameter (see Appendix A).

An alternative, more accurate, estimate of the values α_{cn} can be obtained by exploiting the perturbation theory based on the finite gap formulation of the inverse scattering transform for the NLSE [44], which yields a particularly simple formula (details in Appendix A),

$$\alpha_{cn} = \frac{p^2 e_+ e_-}{g} \frac{a^2}{n}, \quad n = 1, 2, 3, \ldots, \quad (4)$$

where e_+ (e_-) are the growing (decaying) eigenvector of MI [15,19], associated with the MI gain $g = g(\omega_0) = \omega_0(4p - \omega_0^2)^{1/2}$. Equation (A15) turns out to be extremely accurate in the limit of small sidebands [i.e., $a = O(\epsilon), \epsilon \ll 1$, which gives $\alpha = O(\epsilon^2)$, see Appendix A] but gives a reasonable approximation also for relatively large sidebands (5%). This is depicted in Fig. 1(d) by the vertical dashed lines corresponding to α_{c1} and α_{c2}.

III. EXPERIMENT

A. Experimental setup

To demonstrate the existence of critical values of damping around which FPUT recurrence is qualitatively affected by the separatrix crossing phenomenon, we exploit a full fiber-optics setup, similar to the one in Refs. [25,32,48,58,59]. This is based on a nondestructive method based on heterodyne optical time domain reflectometer (HOTDR) to resolve multiple recurrences in both power and phase along the fiber [25,48], on top of which we introduce an accurate control of the effective damping.

A simplified sketch of the setup is presented in Fig. 2. A continuous-wave laser emitting at $\lambda = 1550$ nm (cw laser 1)

is intensity modulated to generate a 50 ns square pulses train (repetition rate of 4.9 kHz), which is short enough to avoid stimulated Brillouin scattering and implement OTDR, although long enough to contain a few thousand modulation periods. The phase modulator then shapes the signal into a triangular frequency comb whose laser line frequency spacing is f_m. Then, a Waveshaper, a programmable optical filter, truncates this comb to three waves only, which are tuned in amplitude and phase. Finally, an erbium doped fiber amplifier increases the total power to 528 mW, to achieve the desired nonlinear regime [pump power $P_P(z = 0) = 480$ mW and signal power $P_S(z = 0) = 24$ mW per sideband]. These light pulses then propagate into a 20.15-km-long SMF-28 optical fiber with nonlinear coefficient $\gamma = 1.3$ W^{-1} km^{-1} and group velocity dispersion $\beta_2 = -19$ ps^2 km^{-1}. The pump to signal frequency shift f_m is set to 38.2 GHz, close to the perfect phase matching frequency located at 41 GHz [46].

HOTDR is performed by exploiting a local oscillator (cw laser 2), phase-locked with cw laser 1, and modulated to get a frequency comb with the same line-to-line spacing f_m but detuned by 800 MHz. The power and phase distributions are obtained by heterodyning between the Rayleigh backscattered waves and the multitone local oscillator (see Refs. [25,48] for details). In particular, each backscattered frequency component beats with its own nearest local oscillator spectral line. Two detection channels allow for the simultaneous recording of power and relative phase evolutions of two waves (pump and signal).

A key feature of the setup is the tailoring of the effective loss. To this end, we implemented a counterpropagating Raman pump to actively control the damping by tuning the Raman pump power. In Refs. [25,32,48,58,59], we adjusted the Raman pump power to get an almost fully transparent optical fiber. By neglecting the Raman pump dissipation effect, a simplistic description of the loss compensation process allows us to assume that the Raman amplification term $g_R P_R^{\text{opt}}$ is equal to the fiber loss α [46]. Hence, the optical signal experiences a vanishing effective loss $\alpha_{\text{eff}} \simeq 0$ dB/km during its propagation through the fiber. The compensation is almost perfect because the Raman amplifier always operates in a linear regime because signals to amplify are very short [60]. By varying the Raman pump power from 0 mW to P_R^{opt}, we have been able to tune the effective loss α_{eff} in a regime of extremely weak damping ranging from the intrinsic fiber loss value (0.2 dB/km) to 0 dB/km, as illustrated in Fig. 3. For each value of Raman pump, we determine the effective damping as follows. Weak square pulses of 48 mW peak power are launched along the fiber. The nonlinear length Z_{nl} being around 16 km, we can assume that nonlinear effects are negligible. The HOTDR system allows us to monitor their power evolution along the fiber length. As the pulses are mainly affected by dissipation, they experience an exponential decay, as illustrated in Fig. 3(a) with the Raman pump switched off. Note that, in Fig. 3(a), the data cover twice the fiber length since we detect the backscattered signal (the generic distance is traveled forward and then backward before being detected). By fitting the data with an exponential curve [dotted line in Fig. 3(a)], we extrapolate an intrinsic damping coefficient $\alpha_P \simeq 0.2084$ dB/km, in excellent agreement with the data-sheet value of
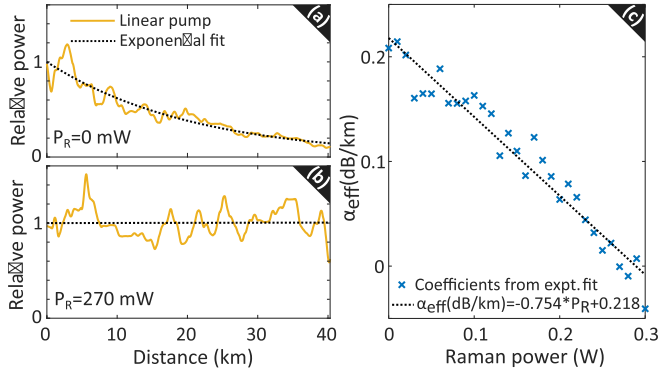
FIG. 3. Power evolution of the backscattered signal, when the Raman pump is (a) switched off, (b) optimized to get a nearly perfect loss compensation. (c) Effective loss α_{eff} versus Raman pump power P_R.

0.2 dB/km. The opposite limit that yields nearly perfect loss compensation for $P_R = P_R^{\text{opt}} = 270$ mW is shown in Fig. 3(b), which shows a quasiflat power profile. We repeat these measurements for Raman pump powers in the range 0–300 mW, with the upper value of 300 mW yielding slight overcompensation (weak gain). The results are summarized in Fig. 3(c), from which we conclude that a nearly linear control of the

loss coefficient can be achieved by tuning the Raman pump power. We make use of the linear fit in Fig. 3(c) to calibrate the effective damping in the successive experiments described below.

B. Experimental results

We have designed the experimental setup in such a way that several recurrences can be observed along the fiber length in order to highlight the impact of weak effective fiber loss on the FPUT process. We have measured the evolution along the fiber of the signal (sideband) power and relative phase for different values of effective loss, keeping the initial pump-signal relative phase to $\Delta\Phi(0) = 0$ (unshifted orbits in the lossless case). The results showing the signal power evolution are summarized in Fig. 4(a). Around optimal compensation ($\alpha_{\text{eff}} = 0$ achieved at $P_R \simeq 270$ mW), four nearly complete recurrence cycles are observed (slightly less than achieved by means of ultralow-loss fibers and stronger input sidebands in Ref. [58]), each featuring a peak conversion followed by the return to the initial condition. The corresponding phase evolution is depicted in Fig. 4(b) and shows nonlinear oscillations around the vanishing (input) phase, which remain bounded in the interval $\pm\pi/2$. This is further clear from the projection of the measured evolution in the phase-plane shown in Fig. 4(c)
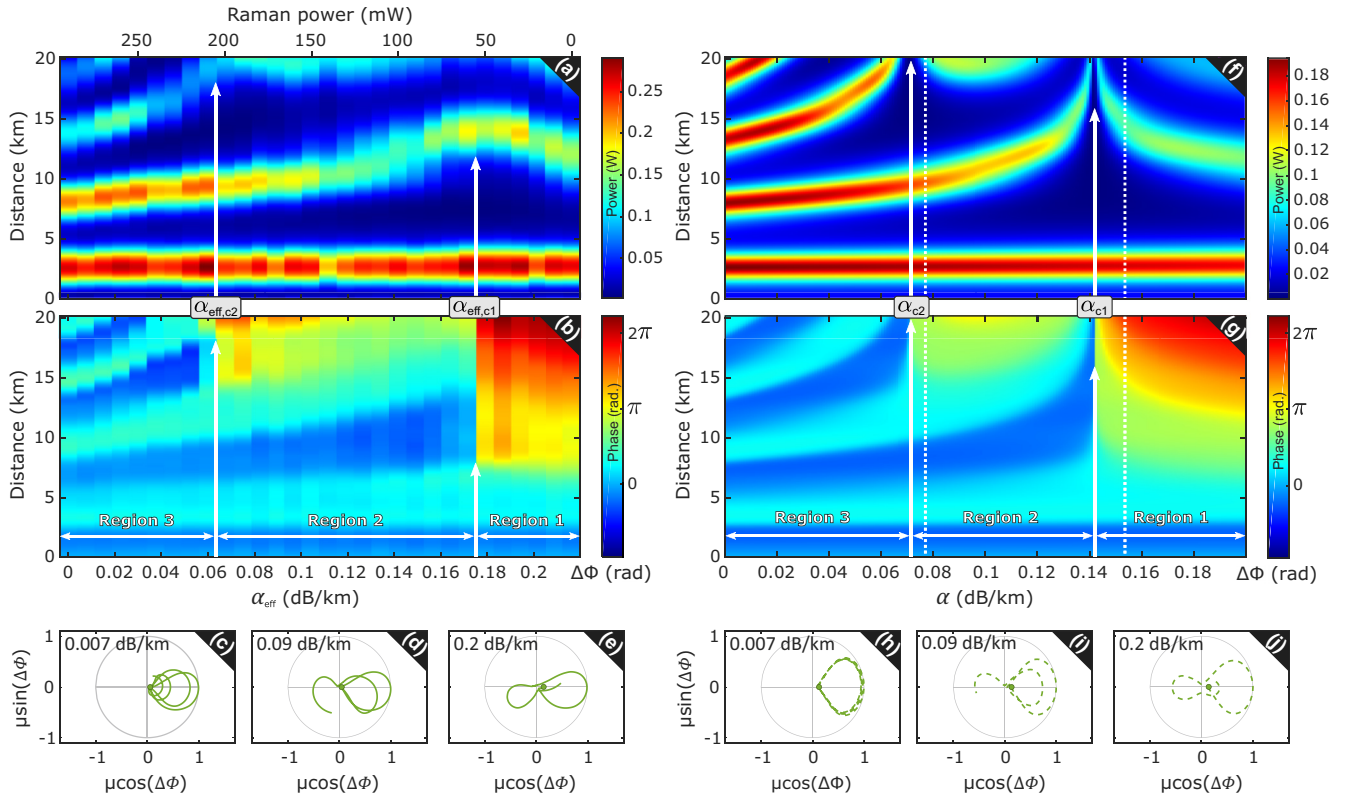

FIG. 4. Left-column panels: Experimental data showing false color plots of (a) signal power and (b) relative phase $\Delta\phi = \phi_P - \phi_S$ in the plane (α_{eff}, Z) of effective loss and fiber distance; (c)–(e) projections of the measured evolutions in the phase plane $(\mu\cos(\Delta\phi), \mu\sin(\Delta\phi))$ for values $\alpha_{\text{eff}}(\text{dB/km}) = 0.007(c), 0.09(d), 0.2(e)$ sampled in regions (1,2,3), respectively. μ stands for the signal power, normalized to the maximum value. Right-column panels (f)–(j) report the numerical counterpart of results in panels (a)–(e), obtained from integration of the damped NLSE [Eq. (1) with $\alpha = \alpha_{\text{eff}}$]; white dotted lines in (f) stand for estimates of α_{c1} and α_{c2} predicted by finite-gap perturbation theory [44].

for the sample value $\alpha_{\mathrm{eff}} = 7 \times 10^{-3}$ dB/km. As shown the trajectory remains bounded in the right semiplane entailing repeated recurrences of the unshifted type.

As the damping increases, a primary observation from Fig. 4(a) is that the first peak conversion (or maximum compression in time) remains basically unchanged at 2.4 km in the whole range of attenuations. This is in excellent agreement with the numerical simulations performed by integrating Eq. (1) and shown in Fig. 4(f), and also fully supported by both perturbation approaches [dotted lines from Eq. (A15), see details in Appendix A]. Indeed, the dissipation has no significant effect on the FPUT process in the first kilometers of the fiber. Conversely, an increasing attenuation has a strong and nontrivial impact on successive (second, third, and fourth) conversion peaks. Initially, at low enough α_{eff}, all such distances for peak conversion get longer when damping increases. Clearly, higher-order recurrences experience a larger rate of growth due to the accumulation of damping over longer distances. Remarkably, however, looking in particular at the third conversion peak, its characteristic distance grows only up to a maximum, where it reaches nearly the fiber end. This condition is reached at the critical value of effective damping $\alpha_{\mathrm{eff},c2} = 0.063$ dB/km corresponding to $P_R = 205$ mW. In the whole range $\alpha_{\mathrm{eff}} \in [0, 0.063]$ dB/km, denoted as region 3 in Fig. 4(a), the first three recurrences are of the unshifted type [i.e., similar to the case in Fig. 4(c)]. However, if we keep on increasing α_{eff} beyond $\alpha_{\mathrm{eff},c2} = 0.063$ dB/km, we notice an inverted trend where the distance of the third peak moderately decreases with increasing losses, as shown in Fig. 4(a) for the experiment and in Fig. 4(f) for the corresponding numerics. Even more importantly, Fig. 4(b) shows that, for $\alpha_{\mathrm{eff}} > \alpha_{\mathrm{eff},c2}$, the third peak conversion is characterized by a π shift of the relative phase. This indicates that, after two complete unshifted recurrences, the third one becomes of the shifted type. This is also consistently displayed by the phase-plane projection of the experimental data reported in Fig. 4(d) [see also Fig. 4(i) for the numerics], obtained for $\alpha_{\mathrm{eff}} = 0.09$ dB/km. In this case, after the second return close to the origin which occurs around $Z = 15$ km, the dynamics follows the double loop (shifted) trajectory, having crossed the separatrix. Importantly, this type of evolution characterizes the whole region 2 corresponding to $\alpha_{\mathrm{eff},c2} < \alpha_{\mathrm{eff}} < \alpha_{\mathrm{eff},c1}$. Here, $\alpha_{\mathrm{eff},c1} = 0.176$ dB/km (obtained at $P_R = 55$ mW), is the characteristic damping where also the second conversion peak undergoes a symmetry breaking. Indeed, the second conversion peak is not critically affected by the previous transition occurring at $\alpha_{\mathrm{eff},c2}$, since its characteristic distance continues to increase smoothly for growing α_{eff}. However, across the damping $\alpha_{\mathrm{eff}} = \alpha_{\mathrm{eff},c1}$, this trend is clearly inverted (the distance starts to decrease for higher α_{eff} above threshold $\alpha_{\mathrm{eff},c1}$), while a characteristic shift of π appears in Figs. 4(b) and 4(g) above threshold. In this case, such transition is associated with the fact that, for $\alpha_{\mathrm{eff}} > \alpha_{\mathrm{eff},c1}$, the dynamics follows the shifted (double-loop) orbits with broken symmetry, right after the first return close to the origin (i.e., the first recurrence). This is shown in Fig. 4(e) [numerics in Fig. 4(j)] for $\alpha_{\mathrm{eff}} = 0.2$ dB/km. The net effect is that, in region 1 ($\alpha_{\mathrm{eff}} > \alpha_{\mathrm{eff},c1}$) only shifted recurrences can be followed, while repeated unshifted recurrences become inaccessible.
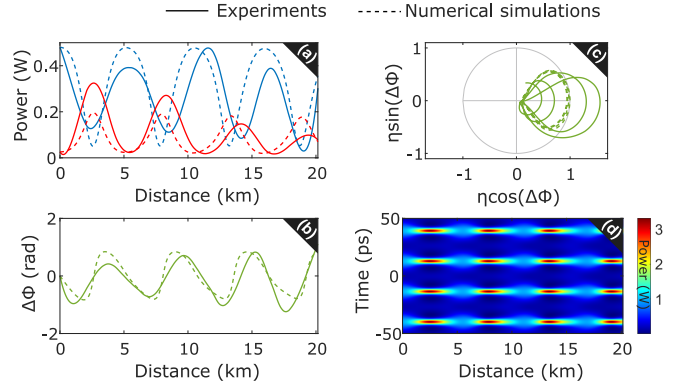

FIG. 5. Evolution, along the fiber length of (a) the pump (blue lines) and the signal (red lines) powers, (b) the relative phase. (c) Phase-plane representation. (d) Numerical spatiotemporal evolution of the power. Solid lines correspond to experimental data, obtained with $P_R = 280$ mW, while dashed lines correspond to numerical simulations, with $\alpha_{\mathrm{eff}} = 0.007$ dB/km (region 3).

Importantly, a good overall agreement is found between the experiment and the numerics in Fig. 4, including the values of the critical losses where $\alpha_{\mathrm{eff},c2} = 0.063$ dB/km and $\alpha_{\mathrm{eff},c1} = 0.176$ dB/km which compares with the numerical values $\alpha_{c2} = 0.071$ dB/km and $\alpha_{c1} = 0.142$ dB/km. We point out that the observation of critical transitions occurring at smaller values of damping and increasing number of recurrences as predicted from theory are prevented by the finite length of the fiber. In turn, operating with longer fiber and fine tuning of much smaller effective losses requires to improve the Raman amplification scheme, which will be addressed in the future.

Further details of the evolutions in the three regimes illustrated in Fig. 4, are illustrated in Figs. 5–7, which explicitly report power and phase evolutions (both measured in the experiment and numerically simulated from the NLSE). In particular, the results presented in Fig. 5 are performed with a quasiperfect compensation of the losses, with $\alpha_{\mathrm{eff}} = 0.007$ dB/km (region 3). The pump and signal power evolutions (blue and red solid lines, respectively) exhibit four sideband peak appearance (slightly less than four recurrences). Importantly, in all the FPUT periods, the experimental relative phase remains bounded (solid green line) in the range $[-\frac{\pi}{2}; \frac{\pi}{2}]$ thus
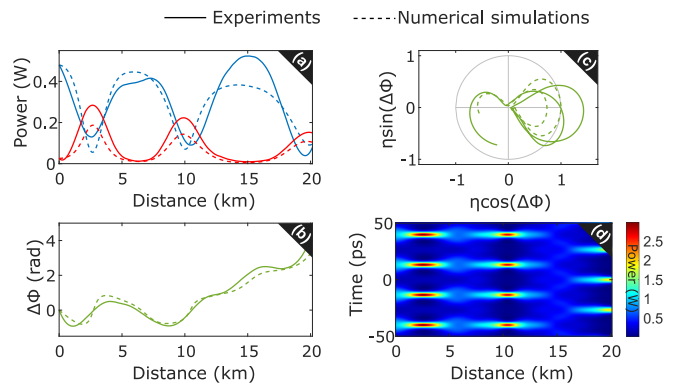

FIG. 6. Same as in Fig. 5. Experimental data are obtained with $P_R = 170$ mW, numerical simulations with $\alpha_{\mathrm{eff}} = 0.09$ dB/km (region 2).
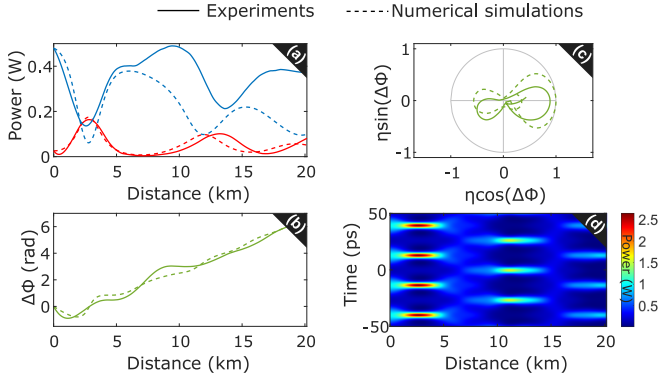
FIG. 7. Same as in Fig. 5. Experimental data are obtained with $P_R = 20$ mW, numerical simulations with $\alpha_{\text{eff}} = 0.2$ dB/km (region 1).

yielding a phase-plane trajectory confined in the right semi-plane. This means that all the recurrences are in phase (the high power pulses appears each time at the same location), as also illustrated by the numerical spatiotemporal evolution of the power in Fig. 5(d).

The results presented in Fig. 6 are relative to $\alpha_{\text{eff}} = 0.09$ dB/km in region 2, obtained with $P_R = 170$ mW. In this case after two peak appearances for which the phase shows bounded oscillations, the third peak appearance is characterized by a phase that increases beyond $\pi/2$, reaches π, and continues to increase monotonically. This denotes that the separatrix has been crossed leading to a shifted orbit (when the phase is π), as also seen from the third high power pulses train π shift in the spatiotemporal evolution of the power.

Finally, the results presented in Fig. 7 show the case of a relatively high effective losses, namely $\alpha_{\text{eff}} = 0.2$ dB/km in region 1. In this case, separatrix crossing occurs right after the first FPUT cycle, since the second peak appearance is already phase shifted.

IV. CONCLUSIONS

In summary, the accurate control of the effective fiber losses performed through Raman amplification techniques has allowed us to demonstrate that the FPUT recurrence due to MI is strongly affected by damping. The main signature is the strong sensitivity of the recurrence periods around critical loss values where separatrix crossing is found to take place. On one hand, this requires to investigate how this phenomenon affects the transition to the thermalized state where FPUT recurrences break down. On the other hand, our findings can be extended to other models, either integrable [51,61,62] or strongly nonintegrable [50,52,63], which present separatrices and an underlying geometric structure of nonlinear MI. Finally, we also point out that similar phenomena of separatrix crossing (though, with inverted role of shifted-unshifted orbits) are envisaged when gain replaces losses [44], which will be addressed in future experiments.

ACKNOWLEDGMENTS

APPENDIX A: PREDICTION OF THE CRITICAL DAMPING COEFFICIENTS

The aim of this section is to show the details of the derivation of the values of the critical damping following either a reduced three-wave mixing (3WM) approach or the finite-gap perturbation theory.

1. The reduced three-wave mixing dynamics

Despite the dissipative nature of the problem, the 3WM approach can lead to a Hamiltonian formulation, although—importantly—of the nonautonomous type. To this end, we find convenient to start from the NLSE in dimensional units

$$i\frac{\partial U}{\partial Z} - \frac{\beta_2}{2}\frac{\partial^2 U}{\partial T^2} + \gamma|U|^2 U = -i\frac{\alpha_P}{2}U. \quad (A1)$$

We consider for the field $U = U(Z, T)$ the following three-wave ansatz (for sake of simplicity, with symmetric sidebands):

$$U = \sqrt{P_0}\left[a_0(Z) + \frac{a_1(Z)}{\sqrt{2}}(e^{i\Omega T} + e^{-i\Omega T})\right]e^{-\frac{\alpha_P}{2}Z}, \quad (A2)$$

where P_0 is the input power, $a_0(Z)$ and $a_1(Z)$ are the complex amplitudes of the pump and sidebands, respectively. Since the last real exponential accounts explicitly for the damping, $a_{0,1}(Z)$ are *undamped* variables, which satisfy power conservation $|a_0|^2 + |a_1|^2 = 1$ at any distance Z. By inserting Eq. (A2) into Eq. (A1), we find, neglecting generation of higher-order sideband pairs at $\pm m\Omega$, $m \geqslant 2$, the following coupled equations:

$$-i\frac{\partial a_0}{\partial Z} = \hat{\gamma}\left[(|a_0|^2 + 2|a_1|^2)a_0 + a_1^2 a_0^*\right], \quad (A3)$$

$$-i\frac{\partial a_1}{\partial Z} = dk a_1 + \hat{\gamma}\left[\left(\frac{3}{2}|a_1|^2 + 2|a_0|^2\right)a_1 + a_0^2 a_1^*\right], \quad (A4)$$

where $dk = \beta_2\frac{\Omega^2}{2}$ is the dispersive mismatch, $\hat{\gamma} \equiv \hat{\gamma}(Z) = \gamma P_0 \exp(-\alpha_P Z) = Z_{nl}^{-1}\exp(-\alpha_P Z)$ is an effective damped (z dependent) nonlinear coefficient, and $Z_{nl} = (\gamma P_0)^{-1}$ stands for the characteristic nonlinear length associated with input power P_0.

By transforming from variables $a_{0,1}(z)$, to the pair of Hamiltonian conjugated variables $\eta(\bar{z}) = |a_1(\bar{z})|^2 = 1 - |a_0(\bar{z})|^2$ and $\Delta\phi(\bar{z}) = \text{Arg}[a_1(\bar{z})] - \text{Arg}[a_0(\bar{z})]$, and introducing the normalized effective distance $\bar{z} = [1 - \exp(-\alpha z)]/\alpha$, where $z \equiv Z/Z_{nl}$ and $\alpha \equiv \alpha_P Z_{nl}$, we cast Eqs. (A3) and (A4) in the following Hamiltonian form:

$$\frac{d\eta}{d\bar{z}} = \frac{\partial H}{\partial \Delta\phi}, \quad \frac{d\Delta\phi}{d\bar{z}} = -\frac{\partial H}{\partial \eta}, \quad (A5)$$

$$H = \eta(1 - \eta)\cos 2\phi + \left[1 - \frac{\omega^2(\bar{z})}{2}\right]\eta - \frac{3}{4}\eta^2. \quad (A6)$$

Equations are of the same form of the unperturbed ($\alpha = 0$) 3WM system [25,56,64], with the fundamental difference that

the system becomes nonautonomous, due to the fact that now the Hamiltonian (energy) $H = H(\eta, \phi, \bar{z})$ turns out to depend on the distance through the single dimensionless parameter $\omega^2(\bar{z}) = \omega_0^2/(1 - \alpha\bar{z})$. Here the input parameter $\omega(\bar{z} = 0) = \omega_0 = \Omega\sqrt{|\beta_2 Z_{nl}|}$ is nothing but the normalized modulation frequency which fully characterizes the unperturbed (undamped) evolutions along with the initial condition in terms of sidebands fraction and overall phase [25]. Importantly, in the presence of damping, the frequency parameter $\omega(\bar{z})$ increases exponentially upon propagation because the total power (at denominator) is exponentially damped. Furthermore, by taking the total derivative of Eq. (A6) and exploiting the Hamiltonian constraint $\frac{\partial H}{\partial \eta}\frac{d\eta}{d\bar{z}} + \frac{\partial H}{\partial \Delta\phi}\frac{d\Delta\phi}{d\bar{z}} = 0$, we obtain the equation that rules the variation of the Hamiltonian along the motion in the form

$$\frac{dH}{d\bar{z}} = \frac{\partial H}{\partial \bar{z}} = -\frac{\alpha}{2}\frac{\omega_0^2}{(1 - \alpha\bar{z})^2}\eta(\bar{z}). \quad (A7)$$

Equation (A7) can be more conveniently rewritten by returning to the evolution variable $z = \alpha^{-1}\ln(1 - \alpha\bar{z})^{-1}$, obtaining

$$\frac{dH}{dz} = -\frac{\alpha}{2}\omega^2(z)\eta(z), \quad \omega^2(z) \equiv \omega_0^2 e^{\alpha z}. \quad (A8)$$

The integration of Eq. (A8) between $z = 0$ and $z = nz_{per}$ (n periods) of the unshifted orbit, with corresponding values of the Hamiltonian $H_0 \equiv H(\eta_0, \phi_0 = 0, z = 0)$ and $H_n \equiv H(nz_{per})$, respectively, yields

$$H_n - H_0 = -\frac{\alpha\omega_0^2}{2}\int_0^{nz_{per}} e^{\alpha z}\,\eta(z)dz, \quad (A9)$$

where the right-hand side (RHS) gives the variation of the Hamiltonian $\Delta H(\alpha) \equiv -\frac{\alpha\omega_0^2}{2}\int_0^{nz_{per}} e^{\alpha z}\,\eta(z)dz$, which can be considered a function of α for fixed initial condition and choice of ω_0. The nth critical value of the attenuation α can be estimated by assuming that the evolution is such that, after n complete unshifted orbits, the point arrives, in the phase plane $(\eta\cos\phi, \eta\sin\phi)$, to its closest approach to the saddle point (i.e., the origin, which represents the MI-unstable pump) with the same energy pertaining to the saddle, i.e., $H_n = H_{saddle} \equiv H(\eta = 0) = 0$. Using Eq. (A9) with $H_n = 0$, the critical attenuations satisfy Eq. (3) of the paper, which we repeat here in implicit form

$$-H_0 = \Delta H(\alpha_{cn}). \quad (A10)$$

To verify Eq. (A10), we have reported in Fig. 8(a) the variation of the Hamiltonian $\Delta H(\alpha)$ [RHS in Eq. (A9)] vs α for $n = 1, 2, 3, 4, 5$. The integral is calculated by using the unperturbed values ($\alpha = 0$) of z_{per} and $\eta(z)$, due to smallness of α. The crossing values with the constant $-H_0$, gives the critical values $\alpha = \alpha_{cn}$, marked by vertical dashed lines in Fig. 8(a). They turn out to be in very good agreement with the values obtained from numerical integration of the damped three-wave equations [Eqs. (A3) and (A4)], reported in Fig. 8(b). Therefore, this simple approach gives a clear insight on the physical mechanism of FPUT separatrix crossing which is behind the existence of the multiple critical losses. From the quantitative point of view, however, the critical values α_{cn} from Eq. (A10) are found to overestimate those arising from
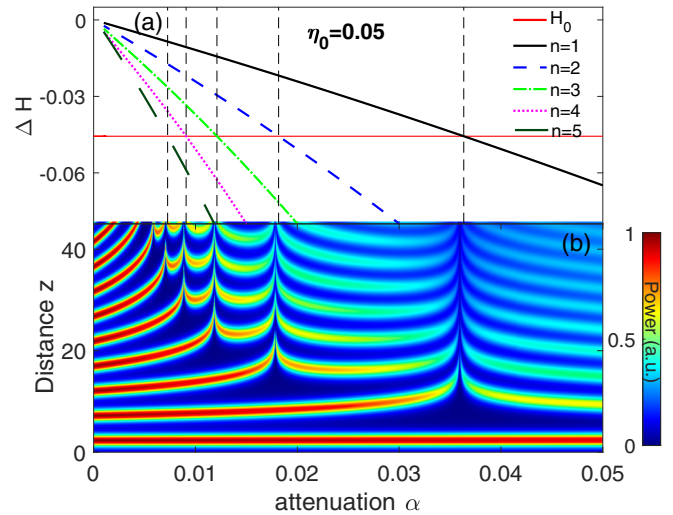

FIG. 8. (a) Variation of the Hamiltonian $\Delta H(\alpha)$ vs attenuation α, for $n = 1, 2, 3, 4, 5$ passages in the unshifted orbit. Vertical dashed lines mark the critical damping values $\alpha = \alpha_{cn}$, given by crossing of $\Delta H(\alpha)$ with $-H_0$ (red horizontal line). (b) False color plot of sidebands power fraction $\eta(z)$ vs α obtained from numerical integration of Eqs. (A3) and (A4). Here $\omega = \sqrt{2}$ and $\eta_0 = 0.05$, as in Fig. 1 of the paper.

the NLSE, due to the fact that the three-wave approximation overestimates the period z_{per} of the recurrence.

2. Perturbative finite-gap approach

Based on a different approach, the impact of losses can be assessed by means of a perturbation theory, developed by Coppini *et al.* in Ref. [44], based on the inverse scattering method for the NLSE with periodic boundary conditions, generally known as finite-gap theory of the NLSE. A convenient form of the initial condition is, in this case,

$$\psi_0 = \sqrt{p}\{1 + \varepsilon[c_1\exp(i\omega t) + c_{-1}\exp(-i\omega t)]\}, \quad (A11)$$

where the perturbation theory requires small sidebands, i.e., $\varepsilon \ll 1$ ($|c_\pm| = O(1)$ accounts for details of the input perturbation, i.e., sideband relative phase and possible imbalance), as well as weak attenuation $\alpha \ll 1$. Without loss of generality, Eq. (A11) becomes identical to the initial condition used in the paper [Eq. (2)] by posing $\varepsilon \equiv a$ and $c_1 = c_{-1} = \exp(-i\phi_0)/\sqrt{2}$.

Under the hypothesis of sufficiently small sidebands and losses, one can derive, despite the complexity of the problem, the following remarkably simple leading-order expression for the distance z_m, $m = 1, 2, 3, \ldots$, at which the mth peak amplification occurs in the recurrent pattern [44]

$$z_m = z_0 + \sum_{n>0}^{m-1}\frac{2}{g}\ln\left(\frac{g^4}{4p^4\varepsilon^2|f_n(\alpha)|}\right), \quad (A12)$$

$$z_0 = \frac{2}{g}\ln\left(\frac{g^2}{2p^2\varepsilon|e_+|}\right), \quad (A13)$$

$$f_n(\alpha) = e_+e_- - n\frac{\alpha}{\varepsilon^2 p^2}g, \quad (A14)$$

where $g = g(\omega_0) = \omega_0(4p - \omega_0^2)^{1/2}$ is the MI gain, and $e_\pm = \exp(\mp i\phi_\omega)c_{\pm 1}^* - \exp(\pm i\phi_\omega)c_{\mp 1}$ stand for the growing and decaying eigenvectors of the linearized stage of MI [15,19], and $\phi_\omega = \cos^{-1}(\omega/2\sqrt{p})$. In Eqs. (A12)–(A14), z_0 stands for the distance of the first peak amplification (i.e., with $m = 1$, $z_1 \equiv z_0$), which coincides with the unperturbed expression obtained with $\alpha = 0$ [15,19], due to the assumption of small attenuation (in other words, for small α, damping has negligible effect over the short distance z_0). Conversely, in Eq. (A12), the nth term of the sum represents the distance Δz_n between the $(n + 1)$st and the nth peak amplifications that emerge upon evolution. In the unperturbed limit $\alpha \to 0$, Δz_n is constant between successive peaks and represents the period of the FPUT recurrence and depends logarithmically on the sidebands through the term $\varepsilon^2 |f_n| = \varepsilon^2 |e_+ e_-|$, consistently with Refs. [15,19,26,65]. Conversely, when $\alpha \neq 0$, due to the additional loss-dependent term on the RHS of Eq. (A14), Δz_n is no longer constant but rather becomes a nonmonotone function of α. As a result, the distances for peak amplification after the first, z_m ($m = 2, 3, 4, \ldots$), as obtained from Eqs. (A12)–(A14), show a marked dependence on the damping coefficient, in qualitative agreement with Fig. 8.

In the framework of this approach, the critical values of attenuation $\alpha = \alpha_{cn}$ are given by the zeros of $f_n(\alpha)$ and hence read explicitly as

$$\alpha_{cn} = \frac{p^2 e_+ e_-}{g} \frac{a^2}{n}, \quad n = 1, 2, 3, \ldots. \quad \text{(A15)}$$

Clearly, for $\alpha = \alpha_{cn}$, $\Delta z_n \to \infty$ instead of becoming very large (compared with the unperturbed value) but finite as shown in Fig. 1 of the paper. Yet, Eq. (A15) constitutes a remarkably accurate estimate of the critical losses α_{cn} for sufficiently weak sidebands, as shown in Fig. 9(a), where we compare, for $\eta_0 = 10^{-3}$, the results obtained from numerical integration of the NLSE with the estimate from Eq. (A15) reported as vertical dashed lines. However, as the sideband amplitude grows larger, the losses in Eq. (A15) are found to overestimate the actual critical losses, as shown in Fig. 9(b) for $\eta_0 = 0.1$, where the relative error turns to be around $\approx 15\% - 19\%$.

APPENDIX B: COMPARISON WITH A DAMPED PENDULUM

The aim of this Appendix is to show that, in spite of the infinite-dimensional nature of the problem, nonlinear MI behaves essentially like the most common of the nonlinear oscillators, namely, the simple pendulum, although with *opposite* reaction to the effect of damping. To show this, let us start from the motion of a standard rigid pendulum in the presence of damping, which is ruled by the following Newtonian equation for the angle $\theta = \theta(t)$ (with respect to the stable equilibrium position) [66]

$$\ddot{\theta} + \frac{\alpha}{2}\dot{\theta} + \omega_0^2 \sin\theta = 0, \quad \text{(B1)}$$

where $\omega_0 = \sqrt{mgh/J}$ is the frequency of the undamped small oscillations, J is the moment of inertia ($J = mh^2$ for a simple pendulum of mass m held at distance h from center of rotation), and α is the normalized energy damping rate
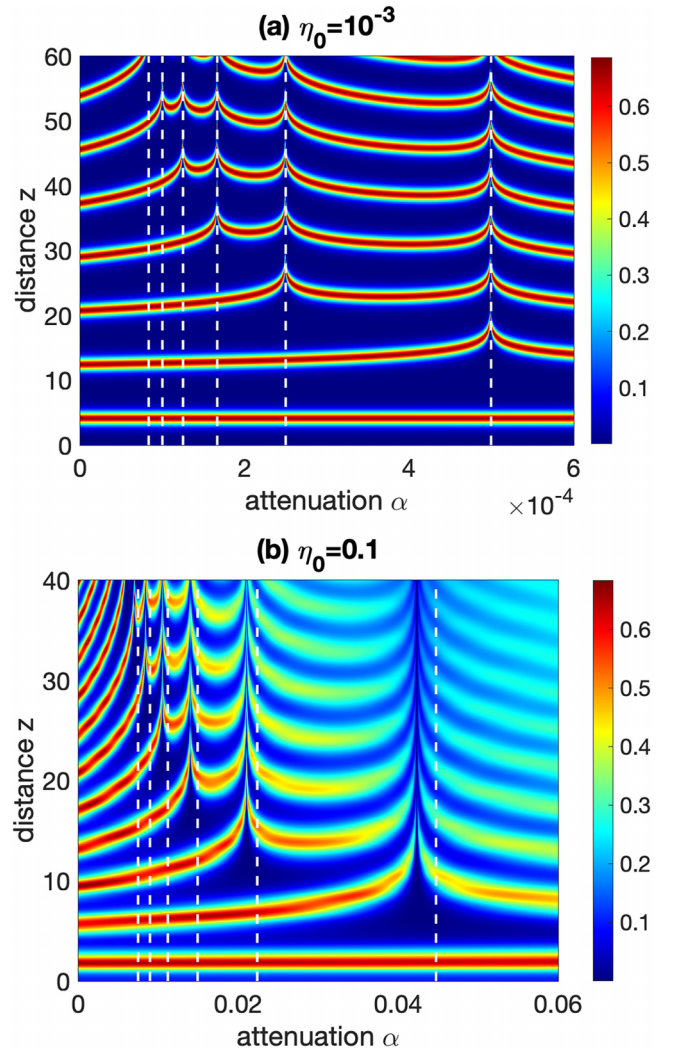

FIG. 9. False color plot of sideband power fraction $\eta(z)$ vs α arising from numerical integration of the NLSE. The critical values of attenuation α_{cn}, which correspond to the maximal distances between successive peaks of $\eta(z)$ are compared with the predictions from Eq. (A15), reported as vertical dashed white lines. Here $\omega = \sqrt{2}$ and the initial sideband power fraction is (a) $\eta_0 = 10^{-3}$ (top), (b) $\eta_0 = 0.1$ (bottom).

due to friction. When $\alpha = 0$, Eq. (B1) gives a Hamiltonian system for conjugated variables $\theta(t)$ and angular velocity $p(t) \equiv \dot{\theta}(t)$, with Hamiltonian (conserved energy) $H_p = p^2/2 - \omega_0^2 \cos\theta$. The level curves of H_p in the plane (θ, p), reported in Fig. 10(b), give the classical phase-plane portrait of the pendulum. We compare such portrait with the phase-plane picture of nonlinear MI shown in Fig. 10(a), which follows from the truncated Hamiltonian H in Eq. (A6) with $\alpha = 0$ (i.e., constant $\omega = \omega_0$). To make the comparison easier, we report the latter in the plane (ϕ, η), where the saddle points in the origin in Fig. 1(a) maps into the saddles $\Delta\phi = \pm\pi/4$, which represent the stable and unstable manifolds of the pump eigenmode $\eta_s = 0$ (at peak gain frequency $\omega_0 = \sqrt{2}$).

The comparison of Fig. 10(a) with Fig. 10(b) clearly show that, in both cases, inner domains (with respect to the separatrices, solid black lines) exist, which describe bounded motion
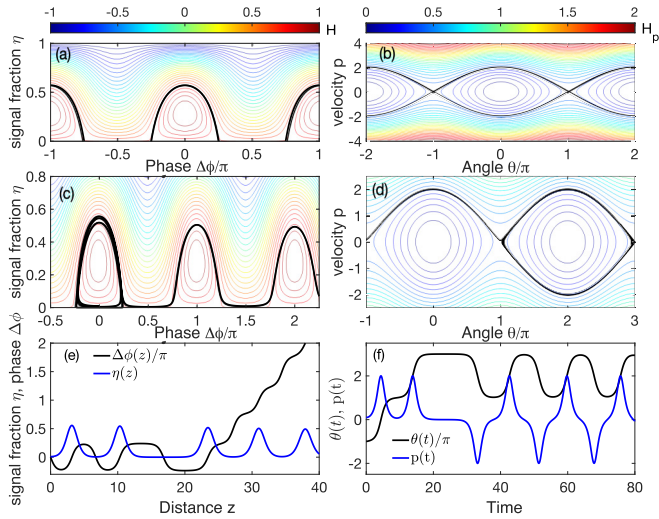
FIG. 10. Comparison between the damped 3WM [left panels (a), (c), (e)] and a damped pendulum [right panels (b), (d), (f)]. Unperturbed phase-plane pictures with black solid line standing for the separatrix [(a) $\omega_0 = \sqrt{2}$, (b) $\omega_0 = 1$]. (c), (d) Projection of the perturbed (by small damping) trajectories (black solid lines) on the relative phase-plane (level curves are unperturbed). Corresponding separatrix-crossing evolutions in terms of variables (e) $\eta(z)$, $\phi(z)$ for MI, and (f) θ, $\dot{\theta}$ for the pendulum. Plot of MI trajectories in panels (c) and (e) are obtained with $\omega_0 = \sqrt{2}$, $\alpha = 4 \times 10^{-3}$, and initially bounded or unshifted orbit (initial condition $\eta_0 = 0.01$, $\Delta\phi_0 = 0$), while for the pendulum $\alpha = 6.2 \times 10^{-4}$, $\omega_0 = 1$ and the orbit is initially unbounded (rotating pendulum, $\theta_0 = -\pi$, $p_0 = \dot{\theta}_0 = 0.1$).

(in angle θ for the pendulum, or phase $\Delta\phi$ for MI). They are separated from outer domains where θ or $\Delta\phi$ are instead

unbounded or free-running. The inner orbits correspond to unshifted evolution of MI and librations of the pendulum, whereas the outer orbits give shifted evolution of MI and pendulum rotations. Notwithstanding the similarity between librations and unshifted orbits on one hand, and rotations and shifted orbits on the other hand, we emphasize, however, that the energetic behavior is opposite for MI and the pendulum. Indeed, as the color bars in Figs. 10(a) and 10(b) indicate, rotations are more energetic (or more nonlinear, so to say) than librations, whereas unshifted orbits are more energetic (nonlinear) than the shifted ones. In turn, this also determines an opposite reaction to the damping. Indeed the losses always induce the energy (Hamiltonian) to decrease. As a consequence, in the pendulum, damping can only induce initial rotations to crossover into librations, but not vice versa. An example where the pendulum switches to librations after two complete rotations is shown in Figs. 10(d) and 10(f). In particular, Fig. 10(d) displays the phase-plane projection of the motion, whereas Fig. 10(f) shows the temporal evolutions of angle and velocity. Conversely, nonlinear MI undergoes damping-induced separatrix-crossing from bounded (unshifted) phase evolutions to unbounded (shifted) ones [see example in Figs. 10(c) and 10(e)]. In particular, the evolution of $\Delta\phi(z)$ in Figs. 10(c) and 10(e) clearly marks the transition from bounded to unbounded motion, in contrast with the evolution of $\theta(t)$ in Fig. 10(f) that exhibits the opposite transition. Therefore, we conclude that FPUT in nonlinear MI in the presence of damping exhibits a reversed behavior compared with a damped pendulum.

Finally, we remark that, even for a simple pendulum, the fine tuning of the damping is challenging, and we are not aware of experimental results that demonstrate a controlled separatrix crossing for such system.

[1] T. B. Benjamin and J. E. Feir, J. Fluid Mech. **27**, 417 (1967).

[2] V. Zakharov and L. Ostrovsky, Physica D (Amsterdam, Neth.) **238**, 540 (2009).

[3] V. I. Bespalov and V. I. Talanov, JETP Lett. **3**, 307 (1966).

[4] K. Tai, A. Hasegawa, and A. Tomita, Phys. Rev. Lett. **56**, 135 (1986).

[5] T. Taniuti and H. Washimi, Phys. Rev. Lett. **21**, 209 (1968).

[6] P. J. Everitt, M. A. Sooriyabandara, M. Guasoni, P. B. Wigley, C. H. Wei, G. D. McDonald, K. S. Hardman, P. Manju, J. D. Close, C. C. N. Kuhn, S. S. Szigeti, Y. S. Kivshar, and N. P. Robins, Phys. Rev. A **96**, 041601(R) (2017).

[7] D. Leykam, E. Smolina, A. Maluckov, S. Flach, and D. A. Smirnova, Phys. Rev. Lett. **126**, 073901 (2021).

[8] J. M. Dudley, F. Dias, M. Erkintalo, and G. Genty, Nat. Photonics **8**, 755 (2014).

[9] M. Onorato, S. Residori, U. Bortolozzo, A. Montina, and F. Arecchi, Phys. Rep. **528**, 47 (2013).

[10] V. E. Zakharov and A. A. Gelash, Phys. Rev. Lett. **111**, 054101 (2013).

[11] G. Biondini and D. Mantzavinos, Phys. Rev. Lett. **116**, 043902 (2016).

[12] J. M. Soto-Crespo, N. Devine, and N. Akhmediev, Phys. Rev. Lett. **116**, 103901 (2016).

[13] A. Armaroli, M. Brunetti, and J. Kasparian, Phys. Rev. E **96**, 012222 (2017).

[14] A. Armaroli, D. Eeltink, M. Brunetti, and J. Kasparian, Phys. Fluids **30**, 017102 (2018).

[15] P. Grinevich and P. Santini, Phys. Lett. A **382**, 973 (2018).

[16] P. G. Grinevich and P. M. Santini, Nonlinearity **31**, 5258 (2018).

[17] G. Biondini, S. Li, D. Mantzavinos, and S. Trillo, SIAM Rev. **60**, 888 (2018).

[18] M. Conforti, S. Li, G. Biondini, and S. Trillo, Opt. Lett. **43**, 5291 (2018).

[19] S. Trillo and M. Conforti, Opt. Lett. **44**, 4275 (2019).

[20] M. Conforti, A. Mussot, A. Kudlinski, S. Trillo, and N. Akhmediev, Phys. Rev. A **101**, 023843 (2020).

[21] M. Erkintalo, K. Hammani, B. Kibler, C. Finot, N. Akhmediev, J. M. Dudley, and G. Genty, Phys. Rev. Lett. **107**, 253901 (2011).

[22] A. Mussot, A. Kudlinski, M. Droques, P. Szriftgiser, and N. Akhmediev, Phys. Rev. X **4**, 011054 (2014).

[23] B. Kibler, A. Chabchoub, A. Gelash, N. Akhmediev, and V. E. Zakharov, Phys. Rev. X **5**, 041026 (2015).

[24] M. Närhi, B. Wetzel, C. Billet, S. Toenger, T. Sylvestre, J.-M. Merolla, R. Morandotti, F. Dias, G. Genty, and J. M. Dudley, Nat. Commun. **7**, 13675 (2016).

[25] A. Mussot, C. Naveau, M. Conforti, A. Kudlinski, F. Copie, P. Szriftgiser, and S. Trillo, Nat. Photonics **12**, 303 (2018).

[26] D. Pierangeli, M. Flammini, L. Zhang, G. Marcucci, A. J. Agranat, P. G. Grinevich, P. M. Santini, C. Conti, and E. DelRe, Phys. Rev. X **8**, 041017 (2018).

[27] A. Gelash, D. Agafontsev, V. Zakharov, G. El, S. Randoux, and P. Suret, Phys. Rev. Lett. **123**, 234102 (2019).

[28] A. E. Krauch, P. Suret, G. El, and S. Randoux, Phys. Rev. Lett. **122**, 054101 (2019).

[29] A. E. Krauch, D. Agafontsev, S. Randoux, and P. Suret, Phys. Rev. Lett. **123**, 093902 (2019).

[30] J.-W. Goossens, H. Hafermann, and Y. Jaouën, Sci. Rep. **9**, 18467 (2019).

[31] A. U. Nielsen, Y. Xu, C. Todd, M. Ferré, M. G. Clerc, S. Coen, S. G. Murdoch, and M. Erkintalo, Phys. Rev. Lett. **127**, 123901 (2021).

[32] G. Vanderhaegen, C. Naveau, P. Szriftgiser, A. Kudlinski, M. Conforti, A. Mussot, M. Onorato, S. Trillo, A. Chabchoub, and N. Akhmediev, Proc. Natl. Acad. Sci. USA **118**, e2019348118 (2021).

[33] A. Gelash, G. Xu, and B. Kibler, Phys. Rev. Res. **4**, 033197 (2022).

[34] A. Chabchoub, N. P. Hoffmann, and N. Akhmediev, Phys. Rev. Lett. **106**, 204502 (2011).

[35] O. Kimmoun, H. C. Hsu, H. Branger, M. S. Li, Y. Y. Chen, C. Kharif, M. Onorato, E. J. R. Kelleher, B. Kibler, N. Akhmediev, and A. Chabchoub, Sci. Rep. **6**, 28516 (2016).

[36] D. Eeltink, A. Armaroli, C. Luneau, H. Branger, M. Brunetti, and J. Kasparian, Nonlinear Dyn. **102**, 2385 (2020).

[37] F. Bonnefoy, A. Tikan, F. Copie, P. Suret, G. Ducrozet, G. Prabhudesai, G. Michel, A. Cazaubiel, E. Falcon, G. El, and S. Randoux, Phys. Rev. Fluids **5**, 034802 (2020).

[38] G. Xu, A. Chabchoub, D. E. Pelinovsky, and B. Kibler, Phys. Rev. Res. **2**, 033528 (2020).

[39] G. Van Simaeys, P. Emplit, and M. Haelterman, Phys. Rev. Lett. **87**, 033902 (2001).

[40] E. Fermi, J. R. Pasta, and S. Ulam, Studies of Nonlinear Problems, I,Tech. Rep. (Los Alamos Report No. LA-1940, 1955).

[41] M. Onorato, L. Vozzella, D. Proment, and Y. V. Lvov, Proc. Natl. Acad. Sci. USA **112**, 4208 (2015).

[42] Y. V. Lvov and M. Onorato, Phys. Rev. Lett. **120**, 144301 (2018).

[43] G. Vanderhaegen, P. Szriftgiser, A. Kudlinski, M. Conforti, A. Armaroli, and A. Mussot, Phys. Rev. A **106**, 033519 (2022).

[44] F. Coppini, P. G. Grinevich, and P. M. Santini, Phys. Rev. E **101**, 032204 (2020).

[45] C. M. Schober and A. L. Islas, Front. Phys. **9**, 633890 (2021).

[46] G. Agrawal, *Nonlinear Fiber Optics* (Academic Press, 2007).

[47] J. D. Ania-Castañón, T. J. Ellingham, R. Ibbotson, X. Chen, L. Zhang, and S. K. Turitsyn, Phys. Rev. Lett. **96**, 023902 (2006).

[48] C. Naveau, G. Vanderhaegen, P. Szriftgiser, G. Martinelli, M. Droques, A. Kudlinski, M. Conforti, S. Trillo, N. Akhmediev, and A. Mussot, Front. Phys. **9**, 637812 (2021).

[49] H. Segur and D. M. Henderson, Eur. Phys. J. Spec. Top. **147**, 25 (2007).

[50] M. Conforti, A. Mussot, A. Kudlinski, S. Rota Nodari, G. Dujardin, S. De Biévre, A. Armaroli, and S. Trillo, Phys. Rev. Lett. **117**, 013901 (2016).

[51] C. Liu, Y.-H. Wu, S.-C. Chen, X. Yao, and N. Akhmediev, Phys. Rev. Lett. **127**, 094102 (2021).

[52] X. Yao, C. Liu, Z.-Y. Yang, and W.-L. Yang, Phys. Rev. Res. **4**, 013246 (2022).

[53] N. Akhmediev and V. I. Korneev, Theor. Math. Phys. **69**, 1089 (1986).

[54] N. Akhmediev, V. M. Eleonskii, and N. E. Kulagin, Theor. Math. Phys. **72**, 809 (1987).

[55] E. Kuznetsov, Sov. Phys. Dokl. **22**, 507 (1977).

[56] S. Trillo and S. Wabnitz, Opt. Lett. **16**, 986 (1991).

[57] S. Trillo and S. Wabnitz, Opt. Lett. **16**, 1566 (1991).

[58] G. Vanderhaegen, P. Szriftgiser, A. Kudlinski, M. Conforti, S. Trillo, M. Droques, and A. Mussot, Opt. Express **28**, 17773 (2020).

[59] G. Vanderhaegen, P. Szriftgiser, C. Naveau, A. Kudlinski, M. Conforti, S. Trillo, N. Akhmediev, and A. Mussot, Opt. Lett. **45**, 3757 (2020).

[60] G. Vanderhaegen, P. Szriftgiser, M. Conforti, A. Kudlinski, M. Droques, and A. Mussot, Opt. Lett. **46**, 5019 (2021).

[61] N. Ercolani, M. Forest, and D. W. McLaughlin, Physica D (Amsterdam, Neth.) **43**, 349 (1990).

[62] S.-C. Chen, C. Liu, X. Yao, L.-C. Zhao, and N. Akhmediev, Phys. Rev. E **104**, 024215 (2021).

[63] S. Trillo and S. Wabnitz, Phys. Lett. A **159**, 252 (1991).

[64] G. Cappellini and S. Trillo, J. Opt. Soc. Am. B **8**, 824 (1991).

[65] C. Naveau, P. Szriftgiser, A. Kudlinski, M. Conforti, S. Trillo, and A. Mussot, Opt. Lett. **44**, 5426 (2019).

[66] E. I. Butikov, Eur. J. Phys. **20**, 429 (1999).